Improved Patch-based View Rendering for Focused Plenoptic Cameras with Extended Depth-of-Field

Jose N. Filipe*, Pedro A. A. Assuncao*†, Luis M. N. Tavora†, Rui Fonseca-Pinto*†,
Lucas A. Thomaz*†, and Sergio M. M. Faria*†
*Instituto de Telecomunicações, Portugal, †ESTG, Polytechnic of Leiria, Leiria, Portugal
e-mails: jose.filipe@ieee.org, {amado, lucas.thomaz, sergio.faria}@co.it.pt, {luis.tavora, rui.pinto}@ipleiria.pt

***Abstract*—This paper proposes a patch-based framework to improve view rendering from light fields captured by focused plenoptic cameras with extended depth-of-field. A three-step approach is performed to minimise discontinuities across neighbouring patches and to maximise the information captured from different types of micro-lens. Firstly, the useful patch size of each micro-image is determined to limit the contribution of low light intensity regions into the rendered images. Secondly, anisotropic inpainting is applied to smooth the discontinuities between neighbouring patches. Thirdly, a multi-focus image fusion algorithm is used to efficiently combine the information captured by the different types of micro-lens comprising plenoptic cameras with extended depth-of-field. Significant improvements are obtained in the rendered views, by reducing visible discontinuities between adjacent micro-images, while at the same time increasing the average sharpness of image content by 20%, measured by the Energy of Laplacian (i.e., a focus metric), in comparison to the conventional rendering approach, which always selects the best focused lens type.**

***Index Terms*—Patch-based rendering, Focused plenoptic camera, Extended depth-of-field**

I. Introduction

In recent years, the increasing availability of plenoptic cameras and research advances in light field capture, processing, and rendering, have been contributing for a growing interest in the extended capabilities offered by computational photography. Such capabilities include, for example, changing the point of view, refocusing, rendering all-in-focus images, and computing depth maps from the scene. Unlike traditional single-image acquisition systems, light fields enable promising advances in quite diverse application areas, such as multimedia for entertainment, medical, industry, science, etc.

A crucial step in most light field applications is the view rendering process. Methods for rendering views from focused plenoptic cameras (FPC) are described in the literature, such as [1], [2], where patches of the lenslet image are tiled together to render either refocused image regions or all-in-focus view images. However, these conventional methods have some inherent shortcomings, such as producing visual discontinuities between adjacent patches and discarding potentially useful data by not taking full advantage of visual information captured by different types of lens.

This work was supported by Programa Operacional Regional do Centro, project PLenoISLA POCI-01-0145-FEDER-028325 and by FCT/MCTES through national funds and when applicable co-funded EU funds under the project UIDB/EEA/50008/2020, Portugal.

This paper proposes a new approach to improve the above mentioned limitations of view rendering methods, based on [2], which are the current state of the art used in in FPC. The contribution of this work relies on the view rendering enhancements achieved through three processing steps: (i) computing the maximum patch size to guarantee the use of the most reliable information; (ii) apply anisotropic inpainting to remove discontinuities between patches; (iii) using multi-focus image fusion to efficiently merge the information captured by different types of micro-lens.

The remainder of the paper is organised as follows: Sec. II describes the existing patch-based methods for rendering images from FPC, alongside with their main limitations. In Sec. III, the proposed method is described, and in Sec. IV the achieved results are presented and discussed. Finally in Sec. V, some concluding remarks are drawn.

II. Related Work and Motivation

Focused plenoptic cameras with extended depth-of-field (FPCX) were firstly proposed in [3] to increase the typical narrow depth-of-field of FPC. The distinctive feature of this kind of cameras is that its micro-lens arrays comprises optical elements of different focal lengths.

Rendering views from light fields captured by FPC involves the application of patch-based rendering techniques, such as those proposed in [1]. In [2], a refocusing algorithm is proposed, which consists in choosing a patch of pixels of the same size m from each micro-image, and tiling them together to render the refocused image Ω_m. This process is depicted in Fig. 1, where the lenslet pixels are represented by the whole square grid, the micro-images are represented by the squares with bold sides, and the patches by the coloured squares. It is worthwhile to point out that the relative position of the patches (represented in the figure by the various colours) is maintained in the refocused image shown in the right-hand side.

Using the previously mentioned algorithm, objects beyond the focus plane will exhibit discontinuities between patches due to missing parts, while objects closer than the focus plane will present discontinuities between patches caused by repeated structures [1], [2]. Consequently, since the location of the focus plane is related to the patch size, and an all-in-focus image comprises objects at different depth planes, rendering an extended depth-of-field image requires the use of patches with different sizes. In [2], the optimum patch size,

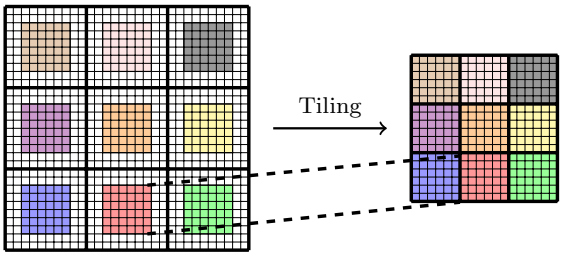

Fig. 1: Illustration of the simple refocusing method [1].

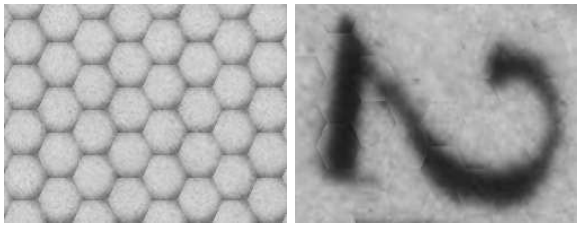

(a) Low light-intensity. (b) Patch borders artifacts.

Fig. 2: Visual effects from the patch-based algorithm [2].

where the scene is in focus, is obtained under the assumption that, in general, images are piece-wise continuous, implying that transitions between patches form neighbour micro-images should also be smooth. Then, the best patch size is chosen based on the minimisation of a gradient-based metric that expresses the continuity between adjacent patches.

The process starts by rendering a focus stack $\Gamma = \{\Omega_m \mid m = 0, ..., M\}$ *i. e.*, a set of images focused at different planes, using the method previously described (M denotes the maximum patch size). In order to emphasise regions with discontinuities, the Laplacian operator $\left(\nabla^2\right)$ is applied to each image belonging to Γ. Then, the gradients for each patch $p_{i,j}$ taken from micro-image $w(i,j)$ are evaluated by integrating along its borders, $b(p_{i,j})$, only considering directions that are perpendicular to the edges. For all images Ω_m, the sum of those orthogonal gradients, σ, is obtained according to (1), where $\hat{n_b}$ denotes a unit vector perpendicular to border b of a given patch $p_{i,j}$, $\cdot$ denotes the inner product, and $\vec{\nabla}$ the gradient operator.

$$\sigma(m,i,j) = \oint_{b(p_{i,j})} \vec{\nabla}\left(\nabla^2 \Omega_m\right) \cdot \hat{n_b}, \qquad \Omega_m \in \Gamma \tag{1}$$

The optimum size is obtained by finding the patch $p_{i,j}$ that presents the smoothest border continuity with its neighbours. For such purpose, a map $z(i,j)$ containing the optimum patch sizes is found through the minimisation of σ, as given by (2),

$$z(i,j) = \underset{m}{\operatorname{argmin}}\ \sigma(m,i,j), \qquad \forall i,j \tag{2}$$

Finally, the extended depth-of-field image is rendered by tiling together the $p_{i,j}$ patches with optimum sizes $z(i,j)$. Since the optimum patches have different sizes, they must be upsampled to the same spatial dimension, in order to allow their concatenation.

In [2], it is suggested to treat each micro-lens type of FPCX as an independent FPC. Therefore, methods typically applied in light fields captured by FPC, can also be used in the case of FPCX.

A. Shortcomings of the rendering process

Despite the gradient minimisation strategy (2), the rendering method previously described yields unavoidable discontinuities across the patch borders of the rendered image for two main reasons: firstly, it does not take into account that lenslet images may exhibit border regions where low light intensity reaches the sensor (i.e., the vignetting effect), which corresponds to a lack of valid information in regions between micro-lenses. Secondly, the process to globally determine the optimal patch sizes cannot avoid the spawning of locally noticeable transitions between adjacent patches after tiling, even when the optimal patch size is chosen. Overall, such patch-based effects contribute to degrade the visual quality of the rendered image, by producing perceptible artefacts. The next paragraphs further detail these two shortcomings of [2].

1) Low light-intensity image regions: lenslet images are generated by capturing the light ray intensity passing through the optical system of a plenoptic camera, comprised of a main lens and a micro-lens array (MLA), placed in front of the camera sensor [4]. Light rays inciding on the central portion of the micro-lenses generate a micro-image, while those impinging on their borders or at interstitial space between micro-lenses are either highly attenuated or blocked, generating invalid information on the sensor. As a result, the lenslet images exhibit darker regions at the micro-images borders.

The rendering algorithm using (2) may find patch dimensions that partially include some of the above mentioned low light-intensity regions, which leads to patch-based artefacts. This is evident in Fig. 2a, which shows a rendered image of a uniform white surface. An uniformly white surface would be expected, but what is observed in Fig. 2a is a visible hexagonal pattern, corresponding to the boundaries of the micro-image patches.

2) Patch border artefacts: although the optimum patch sizes found by the rendering algorithm described in Sec. II tend to produce smooth transitions across patch borders, it is likely that some artificial sharp transitions appear along the matching borders, as can be observed in Fig. 2b. Methods to mitigate this effect were proposed in [5] and [6], but they resort to a depth map computed prior to rendering the extended depth-of-field image. This presents a causality problem as it was noticed by [2], since a depth map is used to render the all-in-focus images, but one of the main goals of the view-rendering process is to convert the light field data to its 4D representation, in order to apply state-of-the-art algorithms for depth calculation.

III. Proposed Method

This section describes the method proposed to overcome the issues described in Sec. II-A. This is implemented as pre and post-processing, in regard to the patch-based rendering algorithm described in [2].

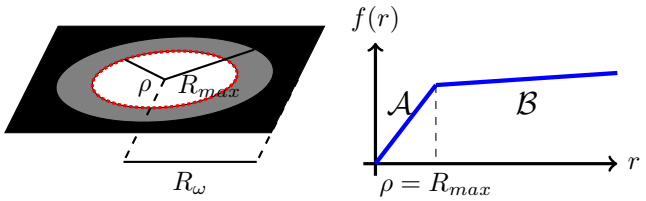

(a) Micro-image w.

(b) Plot of function $f(\rho)$.

Fig. 3: Maximum patch size of a micro-image (3).

A. Estimating the maximum patch size

The first step of the proposed method consists of a pre-processing step to estimate the maximum patch size, so that micro-image pixels belonging to low-light intensity regions (Sec. II-A1) are excluded from the rendering process. This is done by taking into account the circular-like geometry of the micro-lens and selecting the largest possible radius that excludes nearly all the low-light intensity regions, for each micro-image.

In order to estimate the maximum radius (R_{max}) to be used in each micro-image $\omega(i,j)$, an auxiliary bi-dimensional binary mask $K(\rho)$ is defined, so that an element $k \in K(\rho)$ is equal to 1 if its radial distance r_k is lower than an arbitrary radius ρ, and 0 otherwise. This corresponds to masking elements located in the outer region of the circle of radius ρ.

To determine R_{max}, a function $f(\rho)$, defined for each micro-image, is used. Such function is given by (3), where $\langle\cdot,\cdot\rangle_F$ denotes the Frobenius inner product and $\omega(i,j)$ is the micro-image located at position (i,j) of a given lenslet image.

$$f_{i,j}(\rho) = \langle \omega(i,j),\ K(\rho) \rangle_F \qquad \forall\, i,j \tag{3}$$

For each micro-image, (3) is used to calculate the sum of all luminance values located inside the circle with radius ρ (Fig. 3), thus the function monotonically increases with ρ (region $\mathcal{A}$ in Fig. 3b). However, due to the low-light intensity occurring at the borders of each micro-image, yielding low luminance (see Fig. 2a), the rate of change of $f(\rho)$ drastically decreases as ρ increases towards R_ω. Given the nature of $f_{i,j}$, the value ρ where the rate of change decreases can be used to establish $\rho = R_{max}$; in particular, this value of ρ is computed as the one that minimises the second derivative of $f_{i,j}$.

B. Patch Border Anisotropic Inpainting

The second step consists of a post-processing operation. As previously mentioned, even when the size of the patches are chosen to ensure smooth transitions between them, some sharp transitions may still occur (see Fig. 2b). To reduce the effect of such artefacts, the proposed method reconstructs the corresponding affected regions using a diffusion model to keep such border transitions as continuous as possible. This process only operates in bounded regions between adjacent patches. Therefore, the main objective of this post-processing is to propagate the accurate information available in the inner parts of the patches, to their outer rim (*e.g., the region defined by two pixels for each side of the patch border*). This is known as diffusion-based image inpainting [7].

Given an image I with a region to be inpainted Ω, an image boundary $\delta\Omega$ and remaining region ϕ, such that $\phi = I - \Omega$, it is possible to propagate the information of region ϕ to fill region Ω by solving a Partial Differential Equation (PDE), ensuring at the same time that the transition between $\delta\Omega$ and Ω is kept continuous. In order to keep sharp edges of objects present in the image, anisotropic diffusion is used [7]. This kind of inpainting is defined in [8] as (4), where ∇ denotes the differential operator and $\mathbf{D}$ denotes the diffusion matrix.

$$\frac{\partial I}{\partial t} = \vec{\nabla} \cdot (\mathbf{D}\vec{\nabla} I) \tag{4}$$

The diffusion matrix $\mathbf{D}$ is based upon an image descriptor [9], which is chosen as the structure tensor [10]. The index ij of the diffusion matrix $\mathbf{D}$ is determined from the eigenvectors $v_1 = [v_{11}, v_{12}]$ and $v_2 = [v_{21}, v_{22}]$ of the structure tensor and their associated eigenvalues λ_1 and λ_2 [11], as shown in (5).

$$D_{ij} = \sum_{n=1}^{2} \lambda_n \cdot v_{ni} \cdot v_{nj} \tag{5}$$

Since it is not practical nor efficient to solve (4) algebraically, widely known numerical methods, such as the finite differences [12] can be used. In summary, the patch border regions (four pixels wide, two pixel for each side of the border) are iteratively reconstructed, by propagating the information from the inner regions of the patches to their borders.

C. Merging Information from the three Types of Lens

Finally, the third step is also a post-processing step to be applied after the previous one. Here, the three types of lens used in the lenslet image acquisition are treated independently, as if three FPC with different focal length MLAs were capturing the exact same scene. Hence, it is possible to render three similar images from a lenslet image, each corresponding to one type of micro-lens. These images only differ on their focus plane and are slightly shifted apart in the horizontal direction. This is due to the fact that lens of different types are aligned in the same row of lens, but in columns side-by-side, having a horizontal offset between them.

In order to take advantage of the three rendered images of the same scene, conventional methods obtain the final extended depth-of-field image as the pixel-wise average of the three images, after correction of the horizontal offset [2]. However, for the purpose of improving the focusing level, this simple averaging process is less effective than choosing the best focused image among the three of them. To this aim, a new algorithm is proposed to select the most focused lens type for each region and combine them into one extended depth-of-field image. This is performed in two steps: firstly, the horizontal offset between the three images generated from each type of lens is corrected through a registration process. Secondly, for each region of the captured scene, the micro-image corresponding to the better focused micro-lens is selected. Then, an image

composed by these in-focus parts of the original three rendered views is created. This method takes better advantage of the available data than simply averaging the three.

1) Image Registration: An efficient algorithm is used to perform image registration [13]. In a first stage, the problem can be reduced to a correlation maximisation problem [13] in the frequency domain, as given by (6),

$$\underset{x_0,y_0}{\operatorname{argmax}} \sum_{u,v} \left(F(u,v) \cdot G^*(u,v) \cdot e^{i \cdot 2\pi \cdot \left(\frac{u \cdot x_0}{M} + \frac{v \cdot y_0}{N}\right)} \right)^2 \quad (6)$$

where $F(u,v)$ and $G(u,v)$ represent the DFT of the images to be registered $f(x,y)$ and $g(x,y)$, (x_0, y_0) is the offset between the two images and N and M are the spatial dimensions of the image.

The DFT of each image is computed after upsampling by a factor of 2. Then, (6) is used to obtain the offset between the images with half-pixel accuracy, providing and estimate of the final result. At this point, equivalent windows of 1,5 by 1,5 pixels, upsampled by an arbitrary factor of ϵ, are compared between the two images, once again using (6). The final step is to recover the two images, by performing the inverse DFT on each one. This way, it is possible to compute the registration of two images with accuracy of $1/\epsilon$, in a memory-efficient manner.

2) Multi-Focus Image Fusion: in order to merge two images of the same scene, $f(x,y)$ and $g(x,y)$, with dimensions of M by N and focused at different depth planes, a binary segmentation map $p(x,y)$ needs to be computed. The values 1 and 0 indicate which image $f(x,y)$ or $g(x,y)$ is the one to be chosen, respectively. Then, the resulting merged image $h(x,y)$ is computed according to (7), where $\odot$ denotes pixel-wise multiplication.

$$h(x,y) = p(x,y) \odot f(x,y) + (1 - p(x,y)) \odot g(x,y) \quad (7)$$

To compute $p(x,y)$, the absolute value of the filtered versions of f and g (f_{filt} and g_{filt}) are calculated using a Laplacian edge detector [14]. Then, the segmentation map is determined for each sliding window of size $(2w+1)\times(2w+1)$, according to (8), $\Delta F = f_{filt} - g_{filt}$. The windowing approach keeps the computation of (8) feasible.

$$\underset{W_{x,y}}{\operatorname{argmax}} \sum_{l=0}^{2w} \sum_{m=0}^{2w} \Delta F(x-w+l, y-w+m) W_{x,y}(l,m) \quad (8)$$

In (8), $W_{x,y}$ is found by solving the optimisation using the simplex method [15], subject to the constraints that the absolute value of the difference between the vertical and horizontal adjacent values of $W_{x,y}$ cannot be greater than a coherence threshold ξ, and $0 < W_{x,y} < 1$. These constraints force the variations of the segmentation map to be smooth. By joining all the sliding windows together, the whole segmentation map $P(x,y)$ is obtained from (9), where $N_w(x,y)$ is the total number of windows that include the point (x,y).

$$P(x,y) = \frac{\sum_{l=-w}^{l=w} \sum_{m=-w}^{m=w} W_{x+l,y+m}(w-l, w-m)}{N_w(x,y)} \quad (9)$$

The last step to obtain $p(x,y)$ is to binarise the segmentation map $P(x,y)$, by rounding each of its values to the nearest integer, either 0 or 1.

It is now possible to use (7) to merge a pair of images. However, in this specific application, it is necessary to merge three, instead of two images. To do so, an intermediary image, which corresponds to the merge of two of the three images, needs to be computed. To obtain the merge of the three images, the same algorithm is applied, but this time to merge this intermediary image and the third image.

IV. Experimental assessment

The performance of the proposed algorithm was evaluated using a set of light field lenslet images, namely Images A to F.[1] The effectiveness of the method proposed for smoothing the patch transitions of the extended depth-of-field images (described in Secs. III-A and III-B) was first numerically evaluated by measuring the sharpness of border patches. This is based upon the gradient of the Laplacian of each patch border $b(p_{(i,j)})$, in rendered all-in-focus images. The sharpness measure is defined by the smoothness gain $G_q = q(I^{(p)})/q(I^{(r)})$, where q is obtained from (10) for both $I^{(p)}$ (image rendered using the proposed method) and $I^{(r)}$ (image rendered using the reference method [2]).

$$q(I^{(x)}) = \sum_{i,j} \oint_{b(p_{i,j})} \vec{\nabla} \left(\nabla^2 I^{(x)}_{i,j} \right) \cdot \hat{n_b}, \; x \in \{p, r\} \quad (10)$$

Higher values of q mean sharper border transitions and, consequently, lower rendering performance. Therefore higher values of G_q means that patch border transitions of the proposed method are of smaller magnitude than the reference. Additionally, visual observation of rendered images was also considered for further validation.

Table I presents the values of G_q for images A to F, obtained from applying the proposed methods of anisotropic inpainting and maximum patch radius limitation (Secs. III-A and III-B). These results show that the proposed approach significantly reduces the overall accumulated gradient over patch borders by many orders of magnitude. In other words, these processing steps efficiently smooth out the artefacts created by the conventional rendering method. A visual inspection of Fig. 5 and Fig. 4b in comparison to Fig. 2b, show that the inpainted images indeed do not exhibit visible discontinuities along their patch borders, like the images rendered with the reference algorithm. In fact, these discontinuities are reduced by a factor of 379, according with Table I. However, inspection of these figures might give the illusion that the proposed method render more blurred images. Upon close inspection of the border of the "i" in Fig. 5, it is possible to conclude that they are not more blurred when rendered with the proposed method. The illusion of blurdness is given by the removal of the discontinuities between patches. Furthermore, visual results similar to those of Fig. 4 were achieved for all images.

[1] Images available at: https://gitlab.com/plenoisla/EUSIPCO2020Images

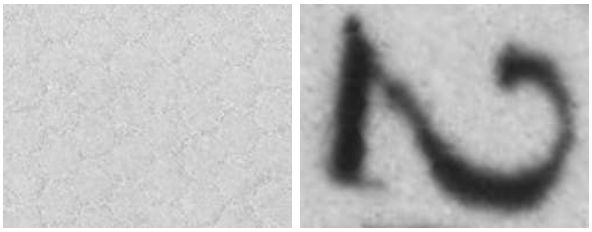

(a) Low light-intensity. (b) Patch borders.

Fig. 4: Proposed method enhancements (Image A).

Image	**A**	**B**	**C**	**D**	**E**	**F**	**Average**
G_q	111	98	624	986	350	106	379

TABLE I: Smoothness gain, G_q of the proposed method.

A second evaluation measure was used for the performance merging algorithm. A comparative focus metric G_F, was defined based on the Energy of Laplacian focus metric $f(\cdot)$, given by (11). I_0, I_1, and I_2 denote the extended depth-of-field images rendered from lens types 0, 1, and 2, respectively. $I_i \in \{I_0, I_1, I_2, I_{merged}\}$, where I_{merged} denotes the merged image rendered from the other three, using the method described in this section.

$$G_f = \frac{f(I_i)}{\max(f(I_0), f(I_1), f(I_2))} \cdot 100 \qquad (11)$$

Table II shows the metric (11) applied to the same set of images[1]. The proposed method outperforms the image rendered with the best focused lens type in all cases. It can be seen that the image I_{merged} yields, in all cases, values higher than 100, meaning that the rendered image is better focused than the image rendered with the reference method. On average, images rendered with the proposed method are 20% sharper than the most focused lens type, according to the Energy of Laplacian metric. These results allow to demonstrate the ability of the proposed merging method to exploit the different types of lenses provided by FPCX, when compared to the reference method.

V. Conclusions

In this work, a method for improving patch-based rendering of all-in-focus images from FPCX was presented, comprised of three complementary steps capable of overcoming the limitations of current algorithms, namely: finding the maximum valid patch size of each micro-image, an inpainting technique,

Image	I_0	I_1	I_2	I_{merged}
A	71	81	100	129
B	68	89	100	117
C	75	100	86	124
D	86	92	100	109
E	66	100	94	111
F	80	85	100	127
Average	74	91	96	120

TABLE II: Assessment of the focus improvement using (11).

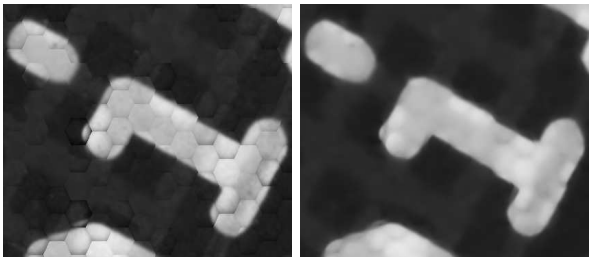

(a) Method of [2]. (b) Proposed method.

Fig. 5: Rendered images (Image B).

and an image fusion method. The simulations results performed for a set of plenoptic images show that the proposed algorithm reduces, on average, the discontinuities between edges of the patches by a factor of 379 while also increasing the overall focus level of the final rendered image by 23%, on average. Thus, the proposed method clearly improves the current state of art on image rendering from FPCX, efficiently exploiting the three different types of lens in such cameras.

References

[1] T. Georgiev and A. Lumsdaine, "Focused plenoptic camera and rendering," *J. Electronic Imaging*, vol. 19, no. 2, p. 021106, 2010.

[2] S. Wanner, J. Fehr, and B. Jähne, "Generating EPI representations of 4D light fields with a single lens focused plenoptic camera," in *Advances in Visual Computing*, G. B. et al., Ed. Berlin: Springer, 2011, pp. 90–101.

[3] C. Perwass and L. Wietzke, "Single lens 3D-camera with extended depth-of-field," in *SPIE*, vol. 8291, 2012, pp. 45 – 59.

[4] M. Harris, "Focusing on everything," *IEEE Spectrum*, vol. 49, no. 5, pp. 44–50, May 2012.

[5] T. Georgiev and A. Lumsdaine, "Reducing plenoptic camera artifacts," *Computer Graphics Forum*, vol. 29, no. 6, pp. 1955–1968, 2010.

[6] P. Liu and R. Zhang, "Artifacts Reduction in Image Rendering of the Focused Plenoptic Camera," in *International Conference on Intelligent Systems Research and Mechatronics Engineering*, vol. 121, 2015, pp. 1292–1297.

[7] C. Guillemot and O. L. Meur, "Image inpainting : Overview and recent advances," *IEEE Signal Processing Magazine*, vol. 31, no. 1, pp. 127–144, Jan. 2014.

[8] Y.-L. You, W. Xu, A. Tannenbaum, and M. Kaveh, "Behavioral analysis of anisotropic diffusion in image processing," *IEEE Transactions on Image Processing*, vol. 5, no. 11, pp. 1539–1553, Nov. 1996.

[9] J. Weickert, "Anisotropic diffusion in image processing," Ph.D. dissertation, Universität Kaiserslautern, Jan. 1996.

[10] J. Bigun, "Optimal orientation detection of linear symmetry," in *IEEE First International Conf. on Computer Vision*, London, Great Britain, June 1987, pp. 433–438.

[11] D.-J. Kroon, C. H. Slump, and T. J. J. Maal, "Optimized anisotropic rotational invariant diffusion scheme on cone-beam ct," in *Medical Image Computing and Computer-Assisted Intervention*. Berlin, Germany: Springer, 2010, pp. 221–228.

[12] C. Grossmann, H.-G. Roos, and M. Stynes, *Numerical treatment of partial differential equations. Revised translation of the 3rd German edition of 'Numerische Behandlung partieller Differentialgleichungen' by Martin Stynes*. Berlin, Germany: Springer, 01 2007.

[13] M. Guizar-Sicairos, S. T. Thurman, and J. R. Fienup, "Efficient subpixel image registration algorithms," *Optics Lettets*, vol. 33, no. 2, pp. 156–158, Jan 2008.

[14] A. Garnica-Carrillo, F. Calderon, and J. Flores, "Multi-focus image fusion by local optimization over sliding windows," *Signal, Image and Video Processing*, vol. 12, no. 5, pp. 869–876, Jul 2018.

[15] G. Dantzig, *Linear Programming and Extensions*, ser. Princeton Landmarks in Mathematics and Physics. Princeton, NJ, USA: Princeton University Press, 2016.